A measurement by BOOMERANG of multiple peaks in the angular power spectrum of the cosmic microwave background

C.B. Netterfield[1], P.A.R. Ade[2], J.J. Bock[3], J.R. Bond[4], J. Borrill[5], A. Boscaleri[6],
K. Coble[7], C.R. Contaldi[4], B.P. Crill[8], P. de Bernardis[9], P. Farese[7], K. Ganga[10],
M. Giacometti[9], E. Hivon[10], V.V. Hristov[8], A. Iacoangeli[9], A.H. Jaffe[11], W.C. Jones[8],
A.E. Lange[8], L. Martinis[9], S. Masi[9], P. Mason[8], P.D. Mauskopf[12], A. Melchiorri[13],
T. Montroy[7], E. Pascale[6], F. Piacentini[9], D. Pogosyan[4], F. Pongetti[9], S. Prunet[4],
G. Romeo[14], J.E. Ruhl[7], F. Scaramuzzi[9]

[1] *Depts. of Physics and Astronomy, University of Toronto, Canada*
[2] *Queen Mary and Westfield College, London, UK*
[3] *Jet Propulsion Laboratory, Pasadena, CA, USA*
[4] *Canadian Institute for Theoretical Astrophysics, University of Toronto, Canada*
[5] *National Energy Research Scientific Computing Center, LBNL, Berkeley, CA, USA*
[6] *IROE-CNR, Firenze, Italy*
[7] *Dept. of Physics, Univ. of California, Santa Barbara, CA, USA*
[8] *California Institute of Technology, Pasadena, CA, USA*
[9] *Dipartimento di Fisica, Universita' La Sapienza, Roma, Italy*
[10] *IPAC, California Institute of Technology, Pasadena, CA, USA*
[11] *Department of Astronomy, Space Sciences Lab and Center for Particle Astrophysics,
University of CA, Berkeley, CA 94720 USA*
[12] *Dept. of Physics and Astronomy, Cardiff University, Cardiff CF24 3YB, Wales, UK*
[13] *Nuclear and Astrophysics Laboratory, University of Oxford, Keble Road, Oxford, OX 3RH, UK*
[14] *Istituto Nazionale di Geofisica, Roma, Italy*

ABSTRACT

This paper presents a measurement of the angular power spectrum of the Cosmic Microwave Background from $\ell = 75$ to $\ell = 1025$ ($\sim 10'$ to 2.4^o) from a combined analysis of four 150 GHz channels in the BOOMERANG experiment. The spectrum contains multiple peaks and minima, as predicted by standard adiabatic-inflationary models in which the primordial plasma undergoes acoustic oscillations. These results, in concert with other types of cosmological measurements and theoretical models, significantly constrain the values of $\Omega_{\rm tot}$, $\Omega_b h^2$, $\Omega_c h^2$ and n_s.

Subject headings: Cosmic Microwave Background Anisotropy, Cosmology

1. Introduction

The presence of a harmonic series of "acoustic" peaks in the angular power spectrum of the cosmic microwave background (CMB) was predicted as early as 1970 (Sunyaev & Zeldovich 1970; Peebles & Yu 1970). These peaks arise due to the evolution of pressure waves in the pre-recombination universe and are a generic feature (Bond and Efstathiou 1987) of most, but not all, cosmological models (e.g., Hu et al. (1997)). Specifically, a well-defined set of peaks is predicted for both adiabatic and some classes of isocurvature models of structure formation, but not for models that rely on topological defects.

Since the COBE measurement of the amplitude of fluctuations in the cosmic microwave background at the largest scales (Bennet et al. 1996), a large literature has developed which predicts, in

the context of adiabatic cold dark matter (CDM) models, the relative position and amplitude of these peaks for different values of the fundamental cosmological parameters. A general prediction of these models is the presence of a dominant fundamental peak at an angular scale $\approx 1^o$ ($\ell \approx 200$), decreasing in angular scale when Ω decreases. Data from a variety of experiments (Miller et al. 1999; Mauskopf et al. 2000; Hanany et al. 2000) including a small fraction of the data from the BOOMERANG 1998/1999 Long Duration Ballooning (BOOM/LDB) campaign (de Bernardis et al. (2000); B00 hereafter) clearly show this feature and provide strong evidence for a low curvature universe, a generic prediction of many inflation models.

There is also convincing evidence that the broad-band average of power at smaller angular scales gradually declines in a manner consistent with adiabatic CDM models (Padin et al. 2001; Church et al. 1997). However, these experiments do not have the necessary combination of sensitivity and sky coverage to convincingly detect or reject the presence of harmonics of the fundamental peak in the power spectrum. The detection of such harmonic peaks would provide strong evidence that the scenario of structure formation from acoustic oscillations in the primordial plasma is accurate.

Present here is an analysis of a larger set of data than previously released from the BOOM/LDB (de Bernardis et al. 2000) experiment which shows clear evidence of multiple peaks in the angular power spectrum of the CMB. Data from four separate detectors that each observe 1.8% of the sky are combined. A new data analysis algorithm is used and refined estimates of the beam shape and overall experimental calibration are presented. The spectrum is consistent with low spatial curvature, Λ-dominated adiabatic CDM models.

2. Instrument

BOOMERANG is a Long Duration Balloon (LDB) experiment designed to measure the angular power spectrum of the CMB at degree and sub-degree scales. For a complete description of the instrument see Crill et al. (2001) and Piacentini et al. (2002). Instrument characteristics are summarized in Table 1.

BOOMERANG was launched for its first LDB flight on December 29, 1998 from McMurdo station, Antarctica, and acquired 257 hours of data from an altitude of $\approx$ 39km. BOOMERANG is comprised of a 1.2m off axis parabolic mirror which feeds a cryogenic mm-wave bolometric receiver. Observations are made simultaneously in four unpolarized bands centered at 90 GHz, 150 GHz, 240 GHz and 410GHz.

The telescope is steerable in azimuth by moving the entire gondola, and in elevation by moving an inner frame containing both the receiver and the optics. The illumination of the optics is not modulated by the scan, which minimizes scan synchronous optically generated offsets. Extensive shielding permits observations in the azimuth range $\pm 60^o$ from the anti-sun direction, for all sun elevations experienced in the antarctic ballooning environment.

3. Observations and Calibration

Observations are made by scanning the telescope in azimuth by 60° peak-to-peak at an angular velocity of 2°/s (hereafter 2dps) (for the first half of the flight) or 1°/s (hereafter 1dps) (for the second half of the flight) at fixed elevation. Each day, the elevation is shifted. Observations are made at elevations of 40°, 45°, and 50°. The scans are centered well away from the Galactic plane. Interspersed in the CMB observations are observations of selected point sources near the Galactic plane. The CMB sky coverage is shown in Figure 1.

The results in this paper contain data from the entire BOOM/LDB flight (as compared to the second half only in B00) and incorporate data from 4 150 GHz channels (as opposed to 1 for B00). This was enabled by using the new data analysis techniques described in Section 4 and in Hivon et al. (2001). In addition, the most significant source of systematic uncertainty at multipoles, $\ell > 400$ is the effective beam size (dominated by pointing uncertainties). Since the release of B00, the understanding of the beam and pointing has been significantly improved, allowing computation of the power spectrum out to higher multipoles.

Observations of extra Galactic sources in the main map and scanned observations of bright HII regions near the Galactic plane are used to esti-

TABLE 1

INSTRUMENT CHARACTERISTICS.

Channel	Band (GHz)	NET_{CMB} ($\mu K \sqrt{s}$)	Beam FWHM (')
B150A	148.0 - 171.4	130	9.2 ± 0.5
B150B	145.8 - 168.6	Variable	9.2 ± 0.5
B150A1	145.5 - 167.3	231	9.7 ± 0.5
B150A2	144.0 - 167.2	158	9.4 ± 0.5
B150B1	144.2 - 165.9	196	9.9 ± 0.5
B150B2	143.7 - 164.3	184	9.5 ± 0.5
90 (2 Chs)	79 - 95	140	18 ± 1
240 (3 chs)	228 - 266	200	14.1 ± 1
410 (4 chs)	400 - 419	~ 2700	12.1 ± 1

NOTE.—Summary of relevant instrument characteristics. Only results from the 150GHz channels are presented in this paper. B150B is not used due to non-stationary detector noise. The bandwidth limits are computed to include 68% of the total detected power for a flat spectrum source. The NET is computed at 1Hz.
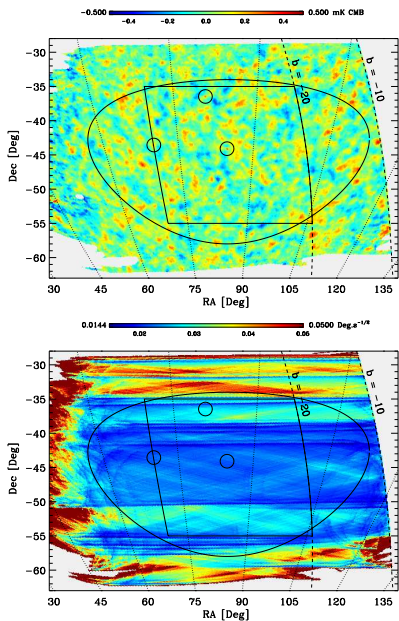

Fig. 1.— Sky coverage. The upper panel shows the BOOMERANG 150GHz map. The locations of the three bright quasars are circled. The sky subset used in B00 (rectangle) and this paper (ellipse) are shown. The bottom panel shows the integration time/pixel. The ellipse for this analysis was chosen to include the well sampled sky, and to avoid the poorly sampled sky

mate the beam full width half maxima (FWHM) for each channel. These values are presented in Table 1. While these observations provide good statistics on the width of the main lobe, the signal to noise of these data are not sufficient to fully characterize the near sidelobe response and deviation from gaussianity of the beam. To obtain a detailed model of the near sidelobe response of the telescope, a physical optics calculation of the beam shape is performed for each channel using the measured position of the horns in the focal plane. To check the precision of the model calculations, a comparison with near field beam maps is made. Azimuthal cuts through the telescope beams are measured to the ~ -20 dB level. While the channels utilizing conical feed horns compare well with the beam map data, a $\sim 10\%$ discrepancy is observed between the calculated and measured FWHM of the photometer beams. In all cases, the measured FWHM are larger than the calculated beam size. This discrepancy is attributed to the multi–moded nature of the Winston concentrators utilized by these channels. For these channels the FWHM are scaled to fit the measurements of RCW38. To correct for the extended nature of the source, the angular extent of RCW38 was measured independently by the ACBAR instrument to be $2.5'$ (Acbar 2001). The two dimensional far-field radiation patterns from the physical optics calculation are then used to generate the window functions for each channel.

3

The telescope pointing is determined using a combination of rate-gyros and an azimuth sun sensor. In order to recover the long time scale pendulations, the gyroscopes are integrated with a 400s time constant. Given the quoted noise in the gyroscopes of less than $8'/\sqrt{hour}$, a pointing uncertainty of less than 2.7' (1σ) is predicted. The Galactic plane point source observations give a pointing uncertainty of 2.5' (1σ). In the analysis, the calculated beam is convolved with the Gaussian approximation of the pointing uncertainty.

The pointing solution has been improved in this analysis (compared with B00) by better use of the pitch and roll rate gyros, and the regression of a thermally dependent offset in the elevation. A re-analysis of the pointing jitter in the B00 pointing solution, utilizing the apparent centroids of point sources along the Galactic plane yields an effective beam size of $12.9 \pm 1.4'$, for the original pointing solution (as compared to the quoted $10' \pm 1'$ used in B00). When the calibration and beam uncertainties are taken into account, the new results lie, bin by bin, within the overall uncertainty of the B00 spectrum, which was restricted to $\ell ¡/= 600$. The B00 results are systematically lower at high ℓ than those presented here, due to the smaller effective beam that was assumed for the B00 analysis. However, it is reassuring to note that correcting the B00 spectrum with the new estimate of the B00 pointing jitter eliminates any residual discrepancy between the new results and the B00 spectrum (de Bernardis et al. 2002).

The gain calibrations of the 150 GHz channels are obtained from observations of the CMB dipole. The data are high-pass filtered with a filter described by $F = 0.5 \left(1 - \cos\left(\frac{\pi\nu}{f_0}\right)\right)$ for $0 < \nu < f_0$ and 1 elsewhere. In order to retain more large-scale information than is needed in the anisotropy analysis, f_0 is set to the relatively low value of 0.01 Hz. To compare with the data, we artificially sample the CMB dipole signal (Lineweaver et al. 1996), corrected for the Earth's velocity around the sun (Stumpff 1980), according to the BOOMERANG scanning, and filter this fake time stream in the same way as the data. The 1dps data is then fit simultaneously to this filtered dipole, a similarly filtered dust emission model (Finkbeiner et al. 1999), an offset and the BOOMERANG 410 GHz data for all data more than 20° below the

Galactic plane. The dipole calibration numbers obtained with this fit are robust to changes in Galactic cut, and to whether or not a dust model is included in the fit; this indicates that dust is not a serious problem for the contamination. They are insensitive to the inclusion of a 410 GHz channel in the fit, which is a general indication that there is no problem with a wide range of systematics such as atmospheric contamination, as these would be traced by the 410 GHz data.

Overall, the calibration of the spectrum has risen by 10% in C_l (5% in ΔT) compared to B00 due to a refinement of the dipole calibration (improved treatment of the time stream filters) and is further raised by a better calculation of the beam sidelobes.

4. Data Analysis

The data are analyzed in four basic steps: i) the reduction of the raw data into pointed and flagged time streams, ii) the estimation of the noise via an iterative map-making algorithm, iii) the estimation of the angular power spectrum via Monte-Carlo calibrated spherical harmonic transforms, and iv) estimation of parameters by likelihood methods. The size and nature of the BOOMERANG data have required the development of new techniques.

In the reduction of the raw bolometer data, the filter response of the detector and associated electronics is deconvolved from the time stream, and transient phenomena (predominantly cosmic rays) are flagged and replaced in the time stream with a constrained realization of the noise. Similarly, the RA/Dec pointing for each channel is reconstructed from the rate gyros, azimuth sun sensor angle, GPS co-ordinates of the package, and the focal plane geometry. Details can be found in Crill et al. (2001).

The receiver noise for each channel is estimated from the raw time stream by iteratively solving simultaneously for the detector noise spectrum $n(f)$ and the maximum likelihood CMB map, $\Delta = (\mathbf{P}^\dagger \mathbf{N}^{-1} \mathbf{P})^{-1} \mathbf{P}^\dagger \mathbf{N}^{-1} \mathbf{d}$. The algorithm used is an approximate Jacobi method:

loop on j

- $\mathbf{n}^{(\mathbf{j})} = \mathbf{d} - \mathbf{P}\tilde{\mathbf{\Delta}}^{(\mathbf{j})} \Rightarrow \mathbf{N}^{(\mathbf{j})-\mathbf{1}} = \langle \mathbf{n}\mathbf{n}^\dagger \rangle^{-\mathbf{1}}$

- $\tilde{\mathbf{\Delta}}^{(\mathbf{j+1})} - \tilde{\mathbf{\Delta}}^{(\mathbf{j})} = \left(\mathbf{P}^\dagger\mathbf{P}\right)^{-\mathbf{1}}\mathbf{P}^\dagger\mathbf{N}^{(\mathbf{j})-\mathbf{1}}\mathbf{n}^{(\mathbf{j})}$

end loop

where is $\mathbf{N}$ is the time-time correlation matrix, $\mathbf{P}$ is the pointing matrix, $\mathbf{d}$ is the time-stream data, and $\mathbf{n}$ is the noise time stream. If the noise is stationary, then $\mathbf{N}^{-\mathbf{1}}$ is diagonal in Fourier space, and multiplication by $\mathbf{N}^{-\mathbf{1}}$ is just a convolution. And multiplication by $\left(\mathbf{P}^\dagger\mathbf{P}\right)^{-\mathbf{1}}\mathbf{P}^\dagger$ represents binning into pixels and dividing by hits per pixel. For details see Prunet et al. (2000). A complete map and noise spectra takes about 15 minutes on an alpha-ev67 computer.

Two closely related estimators were used to recover the underlying CMB power spectrum C_ℓ from the data. Both methods are based on the Monte Carlo Spherical Harmonic Transform (*MASTER*) technique described in Hivon et al. (2001). *MASTER* allows fast and accurate determination of C_ℓ *without* performing the extremely time consuming matrix-matrix manipulations that characterize exact methods and limit their applicability (Borrill (1999)). It can be summarized as follows. The spherical harmonic transform of a naively binned map of the sky is calculated using a fast $\mathcal{O}(N_{pix}^{1/2}\ell)$ method based on the Healpix tessellation of the sphere (Górski et al. 1998). The angular power in the noisy maps, $\tilde{C}_\ell$, can be related to the true angular power spectrum on the full sky, C_ℓ, by the effect of finite sky coverage ($M_{\ell\ell'}$), time and spatial filtering of the maps (F_ℓ), the finite beam size of the instrument (B_ℓ), and instrument noise (N_ℓ) as

$$\left\langle \widetilde{C_\ell} \right\rangle = \sum_{\ell'} M_{\ell\ell'} F_{\ell'} B_{\ell'}^2 \left\langle C_{\ell'} \right\rangle + \sum_{\ell'} M_{\ell\ell'} F_{\ell'} \left\langle N_{\ell'} \right\rangle. \tag{1}$$

The coupling matrix $M_{\ell\ell'}$ is computed analytically, B_ℓ is determined by the measured beam, F_ℓ is determined from Monte-Carlo simulations of signal-only time streams, and N_ℓ from noise-only simulations of the time streams.

The simulated time streams are created using the actual flight pointing and transient flagging. The signal component of the simulated time streams is generated from simulated CMB maps and the noise component from realizations of the measured detector noise $n(f)$. F_ℓ and N_ℓ are determined by averaging over 150 and 200 realizations respectively. Once all of the components are known the estimation is carried out in two ways.

In the first case the power is determined by solving directly for the unbiased estimator C_ℓ of eqn. 1. The uncertainties in the estimated top-hat binned C_ℓ spectrum are measured by averaging over ensembles (typically 400 realizations) of signal+noise simulations created using a best fit model power spectrum obtained from the data. This allows one to calculate the quantities needed to approximate the full likelihood function for the binned C_ℓ, using the formalism of Bond, Jaffe, and Knox (2000).

In the second case a suitable quadratic estimator of the *full sky* spectrum in the *cut sky* variables $\tilde{C}_\ell$ together with it's Fisher matrix is constructed via the coupling matrix $M_{\ell\ell'}$ and the transfer function F_ℓ (Bond, Jaffe, and Knox 1998; Bond et al. 2001). The underlying power is recovered through the iterative convergence of the quadratic estimator onto the maximum likelihood value as in standard Maximum Likelihood (ML) techniques. A great simplification and speed-up is obtained due to the diagonality of all the quantities involved, effectively avoiding the $\mathcal{O}(N^3)$ large matrix inversion problem of the general ML method. The extension of the quadratic estimator formalism to montecarlo techniques such as MASTER have the added advantage that the Fisher matrix characterizing the uncertainty in the estimator is recovered directly in the iterative solution and does not rely on any potentially biased signal+noise simulation ensembles.

The two procedures agree to within a few percent in the estimated values with the quadratic estimator giving slightly more optimal errors (at the 5% level) over the sample variance limited range of the data. The parameter extraction pipeline was run over results from both methods and the two were found to agree to within the numerical accuracy of the fits.

The drawback of using naively binned maps in the pipeline is that the aggressive time filtering completely suppresses the power in the maps below a critical scale ℓ_c Hivon et al. (2001). This results in one or more bands in the power spectrum running over modes with no power and which are

thus unconstrainable. In pratice we deal with this by binning the power so that all the degenerate modes lie within the first band $2 < \ell < 50$ and regularize the power in the band at DMR power in the likelihood analysis. The estimate in the second band $50 \geq \ell < 100$ will be correlated to this regularized value and as such may be also be considered to be biased by a prior theoretical input. We therefore discard the estimates in the first two bands thus avoiding any correlation to the regularizing scheme used to constrain the power on the largest scales.

An area equivalent to 1.8% of the sky was analysed. The region is enclosed in an ellipse with 20 and 12 degree semi-axes centred at $RA = 85$ and $Dec = -46$. The data and simulations were pixelised with 7 arcminute pixels (Healpix $N_{\text{side}} = 512$). The simulations were run at an angular resolution up to $\ell = 1300$.

Inspection of the BOOMERANG maps shows faint stripes of nearly constant declination, (hereafter "isodec" strips) which vary in amplitude and phase between bolometer channels. The striping patterns vary on day time scales, and are not reproduced in simulated maps made with the same scan pattern and best estimated noise correlations from the time stream data.

To eliminate this contaminant, all modes with a small k_{RA} (which corresponds to isodec stripes) are removed with a Fourier filter. While this clearly eliminates isodec stripes, it also filters out CMB signal. This is accounted for by applying the same filter to the simulated maps in the *MASTER* procedure, so that the effects are included in the determination of F_ℓ. The removal of the stripes still permits an unbiased estimate of the power spectrum of the sky, but does cause a considerable increase in the uncertainties at large angular scales.

The inclusion of several channels is achieved by averaging the maps (both from the data, and from the Monte-Carlos of each channel) before power spectrum estimation. Weighting in the addition is by hits per pixel, and by receiver noise at 1Hz. Each channel has a slightly different beam size, which must be taken into account in the generation of the simulated maps. Any inaccuracy in assuming a common B_ℓ in the angular power spectrum estimation is then absorbed into F_ℓ.

The calculation of the full angular power spectrum and covariance matrix for the four good 150 GHz channels of BOOMERANG (57103 pixels and $\approx 216,000,000$ time samples) takes approximately 1 day running on 8 AMD-athlon 800 MHz work stations.

5. Internal Consistency Tests

The BOOMERANG observing strategy allows for a rich set of internal consistency checks, implemented as a variety of difference maps in which the sky signal should cancel. The power spectra of these difference maps are sensitive to improper characterization of the receiver noise, and contamination not fixed to the celestial sphere. The precision of these difference tests are much more powerful than a comparison of the power spectra, since the sample variance contribution to the power spectrum error bars is proportional to the signal found in each bin, which is near zero for the difference maps. The results of these tests are summarized in Table 2.

The most powerful of these tests is to difference the map made from data acquired while scanning at 2dps (the first half of the flight) from data acquired while scanning at 1dps. (the second half of the flight). This test is sensitive to solar and ground pickup, since between the center of the 2dps data and the center of the 1dps data, the sun moves 5° on the sky, and the gondola has moved half way around the continent between the time centroids of the two maps. The test is also sensitive to errors in the deconvolution of the transfer function of the time-domain signal, since the scan speed changes the spatio-temporal mapping of the signals.

This test is performed on each of the five 150 GHz channels individually. Without filtering out the isodec modes as described previously this test is failed. With the filtering, 4 of the 5 channels pass, and 1 of the 5 channels (150B1) shows a small but statistically significant signal. This channel is excluded from subsequent analysis. The isodec removal is applied to all of the channels included in the analysis.

The 1st half - 2nd half difference test is also performed on maps with the four channels combined. At $l < 300$, there is a statistically significant residual in the difference map at the level of

Table 2

TABLE 2

INTERNAL CONSISTENCY TESTS.

Test	Reduced χ^2	$P_>$
B150A 1dps - 2dps	0.91	0.57
B150A1 1dps - 2dps	0.92	0.56
B150A2 1dps - 2dps	1.04	0.41
B150B1 1dps - 2dps	2.73	7×10^{-5}
B150B2 1dps - 2dps	0.60	0.91
4 Ch 1dps - 2dps	1.80	0.02
4 Ch Left - Right	1.21	0.24
(A+A1) - (A2+B2)	0.61	0.90

NOTE.—Reduced χ^2 with 19 degrees of freedom for internal symmetry tests for BOOMERANG. $P_>$ gives the probability of obtaining a χ^2 larger than the one reported. B150B1 fails the test, and is not used in the analysis. The '4 Ch' entries combine maps from B150A, B150A1, B150A2, and B150B2. The 1dps-2dps 4 Ch spectrum fails marginally. This is dominated by 4 bins centered between $l = 150$ and $l = 300$. The mean signal of these 4 bins is $50 \mu K^2$, compared to a signal over the same range of $\approx 4000 \mu K^2$ (see Table 3).

$50 \mu K^2$. Since the signal only appears in the combined channel 1dps - 2dps analysis, this is consistent with a noise term which changes slowly on the sky and is correlated between channels, such as atmosphere. At these angular scales, the CMB signal is $\approx 4000 \mu K^2$. Since the residual signal is small compared to the CMB signal, its effects are neglected.

A test for artifacts specific to particular detectors is made by differencing the map made from combining B150A and B150A1 with the combination of B150A2 and B150B2, and a test for artifacts due to scan-synchronous baselines is made by differencing maps using only the left-going and right-going portions of the scans. There is no evidence of any residual signal in either of these tests, which is again consistent with a noise term that changes slowly on time scales comparable to the scan time.

6. Foregrounds

The comparison of the maps at the 4 different frequencies measured by BOOMERANG is a powerful tool to test for contamination from foregrounds at 150 GHz. At the resolution frequencies probed by BOOMERANG, thermal emission from interstellar dust grains is expected to be the most important foreground (see e.g. Tegmark et al. (2000)). Masi et al. (2001) probes the level of dust in the BOOMERANG maps by correlating BOOMERANG data with a dust template derived from the 3000 GHz IRAS/DIRBE maps (Schlegel et al. 1999; Finkbeiner et al. 1999) and extrapolating the dust dominated 410 GHz signal to 150 GHz using the measured correlations. The deduced power spectrum of dust fluctuations contributes less than 1% to the power spectrum of sky temperature measured at 150 GHz. For this reason Galactic dust contamination is neglected in the following.

Radio point sources are another potential form of contamination in the maps and angular power spectrum. The WOMBAT (1998) radio point source extrapolations are used to estimate the effects of known radio sources in the BOOMERANG fields. The WOMBAT extrapolated fluxes are converted to temperature using a Gaussian beam that is a good approximation of the beam + pixel window function. Assuming that each of the WOMBAT sources is in a separate pixel, the rms contributed by these point sources to the map is calculated. In the C_ℓ power spectrum this should show up as a constant $C_\ell = C_0$ contribution, which is found by using the effective rms contributed by a random distribution of point sources,

$rms^2 = \sum_\ell (2\ell + 1) C_0 W_\ell / (4\pi)$, and the known beam window function W_ℓ. For results quoted in the units of Table 3, this leads to an estimated point source contribution as a function of ℓ of $160(\ell/1000)^2 \mu\text{K}^2$.

However, three quasars are easily identified in the maps and removed. The brightest two of these are also the two highest flux objects in the Wombat catalog in our region; the third quasar is the eighth brightest in the catalog. Removing only the two brightest sources from the catalog and repeating the above analytic estimate leads to a prediction for the contribution of the remaining sources of only $85(l/1000)^2 \mu\text{K}^2$.

The power spectrum is evaluated directly from the maps before and after removing the three quasars. This was done by ignoring pixels within 0.5^o of the quasar position. This cutting induces very small additional bin-bin correlations in the power spectrum, which are negligible given the small area of the cuts. The effect of cutting the three quasars is less than $170\mu\text{K}^2$ at all $\ell < 1000$. This, combined with the analytic estimates above, gives us good confidence that the residual radio point source contamination is far less than the quoted errors at all ℓ.

7. Power Spectra

The results are summarized in Table 4 and Table 3, and in Figure 2 and Figure 3.

The sensitivity of the results to different binnings is explored. Figure 2 and Table 4 summarize the results from two independent analysis using top-hat binning of width $\Delta l = 75$, and offset and overlapping by 50%. Because of this overlap, adgacent points are strongly correlated. This binning is not used in the parameter extraction.

Figure 3 and Table 3 summarized the results from an analysis with non-overlapping top-hat bins of width $\Delta l = 50$. The sources of uncertainty that are included in the errors quoted in Table 3 include sample variance and statistical noise. The former dominates at $\ell <\approx 600$ and the latter at higher ℓ. These uncertainties are only weakly correlated.

Uncertainty in the effective beam-size introduces an additional uncertainty in the power spectrum that is highly correlated across the spectrum. The uncertainty in the effective beam size has con-
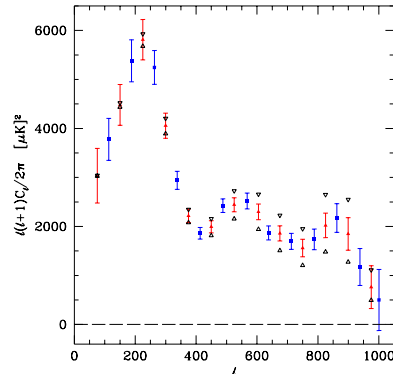

Fig. 2.— The angular power spectrum of the CMB, as measured at 150 GHz by BOOMERANG. The vertical error bars show the statistical + sample variance errors on each point. There is a common 10% calibration uncertainty in temperature, which becomes a 20% uncertainty in the units of this plot. The points are also subject to an uncertainty in the effective beam width of $\pm 1.4'$ (1σ). The effect of a 1σ error in the beam width would be to move the red points (all up together if the beam width has been underestimated, or all down together if the beam width has been overestimated) to the positions shown by the black triangles. The blue points would move in a similar fashion. The blue and red points show the results of two independent analyses using top-hat binnings offset and overlapping by 50%. This shows the basic result is not dependent on binning. While each of the independent spectra (red circles or blue squares) are internally nearly uncorrelated, each red point is highly correlated with its blue neighbors, and vice versa. These data are listed in Table 4

8

TABLE 3

THE ANGULAR SPECTRUM

ℓ range	$\frac{\ell(\ell+1)}{2\pi}C_\ell (\mu K^2)$	(1dps-2dps)/2 (μK^2)	(left-right)/2 (μK^2)	((A+A1)-(A2+B2))/2 (μK^2)
(76 - 125)	3519 ± 558	2 ± 8	− 11 ± 11	4 ± 4
(126 - 175)	4688 ± 555	40 ± 13	− 17 ± 13	3 ± 4
(176 - 225)	5592 ± 548	23 ± 14	− 15 ± 19	− 1 ± 5
(226 - 275)	5699 ± 486	45 ± 19	− 27 ± 25	0 ± 7
(276 - 325)	3890 ± 316	69 ± 24	− 44 ± 33	− 8 ± 9
(326 - 375)	2591 ± 207	10 ± 26	− 32 ± 44	− 9 ± 12
(376 - 425)	1842 ± 152	14 ± 33	− 98 ± 55	− 3 ± 16
(426 - 475)	2070 ± 161	− 58 ± 37	− 90 ± 70	− 8 ± 20
(476 - 525)	2267 ± 174	24 ± 53	− 30 ± 95	23 ± 27
(526 - 575)	2293 ± 182	− 9 ± 68	− 150 ± 118	26 ± 36
(576 - 625)	2058 ± 181	100 ± 93	− 161 ± 155	− 11 ± 43
(626 - 675)	1934 ± 190	28 ± 115	203 ± 217	− 23 ± 56
(676 - 725)	1828 ± 207	− 58 ± 145	71 ± 269	− 32 ± 71
(726 - 775)	1440 ± 226	196 ± 198	− 421 ± 324	89 ± 99
(776 - 825)	1920 ± 288	−336 ± 235	− 808 ± 411	160 ± 131
(826 - 875)	2243 ± 361	−211 ± 317	− 73 ± 580	176 ± 171
(876 - 925)	1752 ± 428	− 94 ± 437	− 613 ± 757	− 23 ± 217
(926 - 975)	985 ± 506	− 78 ± 591	− 607 ± 1013	−458 ± 278
(976 - 1025)	502 ± 627	−128 ± 800	−1370 ± 1347	− 82 ± 395

NOTE.—The spectrum of the CMB, as used in the parameter extraction. The spectrum is further subject to an overall 10% calibration uncertainty, and a 1.4' effective beam uncertainty. The spectrum of the all-channel consistency tests are also given. Adjacent bins are weakly correlated

tributions from uncertainty in the physical beam and from uncertainty in the rms amplitude of the pointing jitter. These combine to produce an uncertainty in the effective beam of ±13%. This uncertainty is not included in the errors quoted in Table 3, as its effect is to produce an overall tilt to the spectrum. The amplitude of the tilt corresponding to the 1 sigma uncertainty that is assigned to the effective beam width is illustrated in Figure 2. This uncertainty is included in the parameter estimation outlined in the next section.

Uncertainty due to instrumental and atmospheric artifacts in the maps are small, based on the internal consistency tests, and are neglected. Similarly, contamination of the maps by both diffuse and compact astrophysical foregrounds are also negligible with respect to the other uncertainties and are neglected.

8. Cosmological Parameters

The angular power spectrum shown in Figure 3 can be used in conjunction with other information to determine cosmological parameters. In this paper, the parameter extraction methods and tools described in detail in Lange et al. (2001) are used.

Specifically, the relative agreement between these data and theoretical predictions over a broad 7-dimensional cosmological parameter space is explored. This parameter space is appropriate for models with adiabatic initial conditions (e.g. inflationary models). The resolution of the second peak virtually rules out alternative models such as defect based scenarios which predict a single broader peak with no secondaries (Turok et al. 1998; Contaldi et al. 1999).

Parameters explored include those describing energy densities, including the total energy density Ω_{tot}, the vacuum energy density Ω_Λ, and the physical densities of baryons and cold dark matter, $\Omega_b h^2$ and $\Omega_c h^2$ respectively. The power spectrum of initial adiabatic density fluctuations is described by a normalization $\ln \mathcal{C}_{10}$ and a power law exponent n_s. The effects of recent reionization of the universe on the observed angular power spectrum, parameterized by the optical depth to decoupling, τ_C, are also explored. For this parameter, the liklihood does not fall sufficiently by the edge of the explored parameter range ($\tau_c < 0.5$) to produce significant limits, though a preference for low values of tau_c are evident in Figure 4.

Given the data, likelihoods as a function of

9

TABLE 4

THE ANGULAR SPECTRUM

ℓ range	$\frac{\ell(\ell+1)}{2\pi}C_\ell(\mu K^2)$
(50 - 113)	3035 $\pm$ 557
(75 - 150)	3776 $\pm$ 428
(112 - 187)	4481 $\pm$ 416
(150 - 225)	5380 $\pm$ 429
(187 - 262)	5810 $\pm$ 413
(225 - 300)	5245 $\pm$ 345
(262 - 337)	4056 $\pm$ 257
(300 - 375)	2942 $\pm$ 184
(337 - 412)	2218 $\pm$ 140
(375 - 450)	1861 $\pm$ 119
(412 - 487)	1992 $\pm$ 123
(450 - 525)	2424 $\pm$ 138
(487 - 562)	2443 $\pm$ 142
(530 - 605)	2520 $\pm$ 162
(567 - 642)	2298 $\pm$ 160
(600 - 675)	1868 $\pm$ 144
(637 - 712)	1858 $\pm$ 154
(675 - 750)	1696 $\pm$ 163
(712 - 787)	1560 $\pm$ 179
(750 - 825)	1736 $\pm$ 211
(787 - 862)	2021 $\pm$ 250
(825 - 900)	2172 $\pm$ 292
(862 - 937)	1847 $\pm$ 333
(900 - 975)	1174 $\pm$ 377
(937 - 1012)	762 $\pm$ 437
(963 - 1038)	499 $\pm$ 623

NOTE.—The spectrum of the CMB, as shown in Figure 2. These are the the results of two independent analyses using $\Delta l = 75$ top-hat binnings offset by $\Delta l = 75/2$ and thus overlapping by 50%. While each of the independent spectra are internally nearly uncorrelated, each red point is highly correlated with its neighbors from the other binning. This binning is not used in the parameter extraction. Rather, the non-overlapping (and thus only weakly correlated) $\Delta l = 50$ top-hat binning listed in Table 3 is. The spectrum is further subject to an overall 10% calibration uncertainty, and a 1.4' effective beam uncertainty.

Table 5

Table 5

Results of Parameter Extraction

Priors	Ω_{tot}	n_s	$\Omega_b h^2$	$\Omega_{cdm} h^2$	Ω_Λ	Ω_m	Ω_b	h	Age
Weak only	$1.02^{0.06}_{0.06}$	$0.96^{0.10}_{0.09}$	$0.022^{0.004}_{0.003}$	$0.13^{0.05}_{0.05}$	$(0.51^{0.23}_{0.20})$	$(0.51^{0.20}_{0.20})$	$0.07^{0.03}_{0.03}$	$(0.56^{0.10}_{0.10})$	$15.2^{1.9}_{1.9}$
LSS	$1.02^{0.04}_{0.05}$	$0.97^{0.10}_{0.08}$	$0.022^{0.004}_{0.003}$	$0.13^{0.03}_{0.02}$	$0.55^{0.09}_{0.09}$	$0.49^{0.12}_{0.12}$	$0.07^{0.02}_{0.03}$	$0.56^{0.09}_{0.09}$	$15.0^{1.3}_{1.3}$
SN1a	$1.02^{0.05}_{0.07}$	$0.99^{0.11}_{0.10}$	$0.023^{0.004}_{0.004}$	$0.10^{0.04}_{0.04}$	$0.73^{0.07}_{0.10}$	$0.31^{0.06}_{0.06}$	$0.06^{0.03}_{0.03}$	$0.61^{0.09}_{0.09}$	$15.9^{2.5}_{2.5}$
LSS & SN1a	$0.99^{0.03}_{0.04}$	$1.03^{0.10}_{0.10}$	$0.023^{0.003}_{0.003}$	$0.14^{0.03}_{0.02}$	$0.65^{0.05}_{0.05}$	$0.34^{0.07}_{0.07}$	$0.05^{0.02}_{0.02}$	$0.67^{0.09}_{0.09}$	$13.7^{1.2}_{1.2}$
$h = 0.71 \pm 0.08$	$0.98^{0.04}_{0.05}$	$0.97^{0.10}_{0.09}$	$0.022^{0.004}_{0.003}$	$0.14^{0.05}_{0.04}$	$0.62^{0.10}_{0.10}$	$0.40^{0.13}_{0.13}$	$0.05^{0.02}_{0.02}$	$(0.65^{0.08}_{0.08})$	$13.7^{1.6}_{1.6}$
Flat	(1.00)	$0.95^{0.09}_{0.08}$	$0.021^{0.003}_{0.003}$	$0.13^{0.04}_{0.04}$	$(0.57^{0.12}_{0.37})$	$(0.48^{0.24}_{0.24})$	$0.06^{0.02}_{0.02}$	$(0.61^{0.13}_{0.13})$	$14.3^{0.6}_{0.6}$
Flat & LSS	(1.00)	$0.98^{0.10}_{0.07}$	$0.021^{0.003}_{0.003}$	$0.13^{0.01}_{0.01}$	$0.62^{0.07}_{0.07}$	$0.38^{0.07}_{0.07}$	$0.05^{0.01}_{0.01}$	$0.62^{0.06}_{0.06}$	$14.5^{0.7}_{0.7}$
Flat & SN1a	(1.00)	$0.98^{0.11}_{0.08}$	$0.022^{0.003}_{0.003}$	$0.12^{0.02}_{0.01}$	$0.68^{0.04}_{0.06}$	$0.33^{0.05}_{0.04}$	$0.05^{0.01}_{0.01}$	$0.66^{0.05}_{0.05}$	$14.0^{0.6}_{0.6}$
Flat, LSS & SN1a	(1.00)	$1.03^{0.10}_{0.09}$	$0.023^{0.003}_{0.003}$	$0.13^{0.01}_{0.01}$	$0.66^{0.06}_{0.06}$	$0.33^{0.05}_{0.05}$	$0.05^{0.01}_{0.01}$	$0.66^{0.05}_{0.05}$	$14.0^{0.6}_{0.6}$

Note.—Results of parameter extraction using successively more restrictive priors, following Lange et al. (2001). The confidence intervals are 1σ. The quoted values are reported after marginalizing over all other parameters. For the primary database parameters, 16% and 84% integrals are reported as $\pm 1\sigma$ errors. For Ω_m, Ω_b, h, and Age, which are functions of the other parameters, the mean and standard deviation over the distribution are reported. All entries are subject to a weak prior in which only models with $0.45 < h < 0.90$ and age > 10 Gyr are considered. The LSS (Bond & Jaffe 1999) and SN1a supernovae (Riess et al. 1998; Perlmutter et al. 1999) priors are as described in Lange et al. (2001). The strong h prior is a Gaussian with the stated 1σ error. Parentheses are used to indicate parameters that did not shift more than 1-σ or have their errors reduced by a factor of two upon the inclusion of the CMB data, compared with an analysis using the priors only. Thus, in these cases the parameter range reflects the choice of prior, rather than a constraint by the CMB. The age column is in units of Gyr.

theoretically predicted power spectra are calculated throughout this parameter space. For every comsological model, beam and calibration uncertainties add two additional parameters. We approximate the possible correction to the beam of effective width ω by a gaussian form $W_\ell(\omega + \delta\omega)/W_\ell(\omega) = e^{-\ell(\ell+1)\omega\delta\omega}$, with $\delta\omega$ assumed to be gaussian distributed with the standard deviation corresponding to $1.4'$. Effectively, every theoretical spectrum is multiplied by $e^{2\ell(\ell+1)\omega\delta\omega}$. Calibration uncertainty of 10% adds to the variance of $\ln \mathcal{C}_{10}$. We do not calculate likelihoods on a grid in beam-width – calibration space, rather for every model we search for a maximum of likelihood in $\delta\omega$ and $\ln \mathcal{C}_{10}$, calculate the curvature of the likelihood near this maximum, and marginalize over the beam and the amplitude by integrating likelihood in the gaussian approximation. The best fit value of $\ln \mathcal{C}_{10}$ and it's variance is used when combining Boomerang predictions with other data.

Parameters are constrained individually by marginalizing over all others, including two describing the calibration and beam window function uncertainties. The 16% and 84% integrals are reported as $\pm 1\sigma$ errors. Other quantities such as the Hubble constant and the age of the Universe are derived from those used to define the parameterization, using the mean and variance over the posterior distribution. The details of the discrete numerical database used for this process, including the limits and values of each parameter tested, and exact prescription used for calculating likelihoods and extracting confidence limits, is fully described in Lange et al. (2001).

Before marginalization, the calculated likelihood for each model is multiplied by the likelihood derived from a series of "prior probabilities", or priors, which represent knowledge from other cosmological measurements. All results considered here have a "weak h + age" top-hat prior applied (hereafter simply the "weak prior") which eliminates models where the universe is younger than 10 Gyr, and limits the Hubble constant, $H_0 = 100\, h\ \mathrm{km\ s^{-1} Mpc^{-1}}$, to $0.45 \leq h \leq 0.9$.

Applying stronger priors in conjunction with this weak prior exercises the ability of the CMB data to combine with other measurements (or theoretical prejudice) to significantly narrow the parameter confidence intervals. Considered here is the impact of applying a stronger constraint on h, constraints derived from measurements of large scale structure (LSS)(Bond & Jaffe 1999), results from recent measurements of type Ia supernovae (Riess et al. 1998; Perlmutter et al. 1999), and the theoretical bias that $\Omega_{\mathrm{tot}} = 1$.
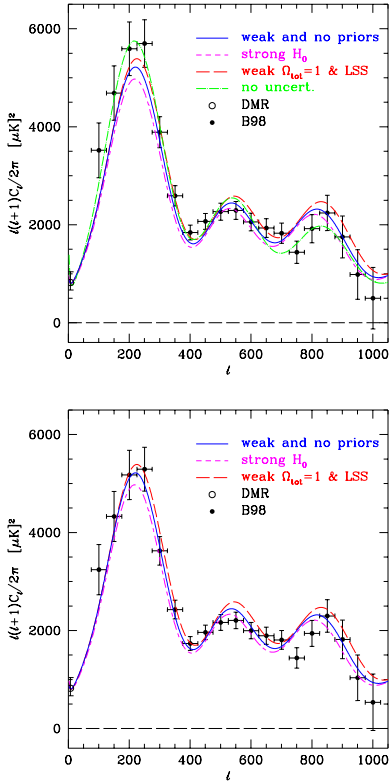
The parameter estimates, given these various

Fig. 3.— Selected best fit models normalized to the best compromise amplitude between COBE-DMR and BOOMERANG are shown overlayed on the BOOMERANG spectrum. The upper panel shows the points plotted as listed in table 3. The best-fit models for the "weak" and "no priors" cases coincide (blue, solid curve) with $\Omega_{tot} = 1.05, H_0 = 50, \Omega_\Lambda = 0.5, \omega_b = 0.020, \omega_c = 0.120, \tau_c = 0, n_s = 0.925, t_0 = 15.8 Gyrs$. Strong Hubble prior gives the best fit model with parameters $\Omega_{tot} = 1., H_0 = 68, \Omega_\Lambda = 0.7, \omega_b = 0.020, \omega_c = 0.120, \tau_c = 0, n_s = 0.925, t_0 = 13.8 Gyrs$. The full analysis takes into account the calibration and beam uncertainties which best fit models take advantage of. This explains the apparent mismatch between some of the models in the upper panel and the plotted central values of Boomerang band powers. The green (dash-dot) curve is the best fit model ($\Omega_{tot} = 1.15, H_0 = 42, \Omega_\Lambda = 0.7, \omega_b = 0.020, \omega_c = 0.060, \tau_c = 0.2, n_s = 0.925, t_0 = 20 Gyrs$) when both beam and calibration uncertainties are switched off. The model fits closely the central values as expected. To demonstrate the effect of beam and calibration uncertanties, in the lower panel the data points have been replotted with a 4% decrease in calibration (0.4σ) and a 0.5 arcminute change in beam size (0.4σ). The plot makes it clear that the best-fit conventional CDM models are indeed good fits to the data, once these uncertainties are correctly accounted for.

combinations of priors, are shown in Table 5, with marginalized likelihood curves for several important parameters given in Figure 4.

Lange et al. (2001) reports a family of models within the database that provide good fits to the angular power spectrum up through $\ell \sim 600$, but represent very young, high baryon density, very closed models outside the normal realm of consideration in modern cosmology. In Lange et al. (2001), the weak prior was used to keep these models from affecting the parameter estimates. Using the power spectrum shown in Figure 3, but limiting consideration to the points with $\ell \leq 600$, similar behavior is exhibited; the very young, high baryon density, very closed models dominate the fits, but can be eliminated by the weak prior. As in Jaffe et al. (2001), adding the higher ℓ points, which exclude models with either a very high or very small third peak, eliminates the high baryon density models. It does not eliminate the closed models in the absence of the weak priors. Thus, just as in Lange et al. (2001), cases with the weak priors applied are the focus of the extraction.
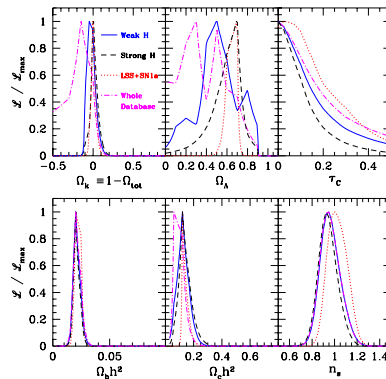

Fig. 4.— Likelihood functions for a subset of the priors used in Table 5. $\Omega_b h^2$, and n_s are well constrained, even under the "whole database" case, and are insensitive to additional priors. Ω_{tot} is poorly constrained over the whole database, but when the weak priors are applied, it becomes stably consistent with the flat case. With the weak priors, Ω_Λ and $\Omega_c h^2$ are poorly constrained, but become significant detections with the addition of the other priors considered. For all cases, τ_c is poorly constrained, but does prefer low values.

As is apparent in Figure 4 and Table 5, $\Omega_b h^2$

and n_s are well localized for all choices of priors. The range for $\Omega_b h^2$ is very consistent with determinations based on Big Bang Nucleosynthesis and measurements of light element abundances (Tytler et al. 2000), while n_s is localized near unity, consistent with inflation-based models. Similarly, once the weak priors are applied, Ω_{tot} is well constrained and consistent with a flat universe. Ω_Λ and $\Omega_c h^2$ are poorly constrained for the weak prior case. τ_C favors low values, but not at a statistically significant level.

These limits agree well with those found in Lange et al. (2001), with one exception. There, the 1σ range for $\Omega_b h^2$ (with the weak prior) is 0.036 ± 0.005. Considering only the points in Figure 3 with $\ell \leq 600$ results in a 1σ limit of 0.027 ± 0.005. This shift is presumably due to the improvement of the pointing solution and smaller error bars compared with B00. The table reflects the estimate made using all points up to $\ell = 1000$; the addition of the information contained in the high-ℓ points has moved the confidence intervals still further.

Having found tight limits on $\Omega_b h^2$, Ω_{tot}, and n_s with the weak priors, the impact of adding other priors can be discussed, to see whether these results are stable (i.e., consistent with the prior) and whether any new parameters can be localized. The table indicates that, in fact, these three parameters are very stable to the addition of the LSS, SN1a, strong h and the theoretically motivated $\Omega_{\text{tot}} = 1$ priors, in various combinations. This insensitivity to choice of priors is a powerful indication that the cosmology is consistent and that these parameters have been robustly determined.

The table also shows that the CMB data can be combined with these priors independently to make statistically significant determinations of Ω_Λ and $\Omega_c h^2$. While the confidence intervals shift somewhat depending on the chosen prior, the rough agreement among these three results, giving $\Omega_\Lambda \sim 0.65$ and $\Omega_c h^2 \sim 0.12$, is very compelling. These LSS and SN1a results are similar to those found in Lange et al. (2001). For the first time, however, the combination of CMB data with just a strong limit on h is powerful enough to yield such a detection.

The table also shows a consistent story for the age of the universe and for the Hubble Constant. For the prior combinations where the limits on h

are dominated by the CMB data rather than the priors, the extraction finds $h \sim 0.65$, with ages between 13 and 15 Gyr. These quantities are most strongly constrained by the CMB data along with the combination of the SN1a prior and flatness.

9. Conclusions

A measurement of the angular power spectrum of the CMB, characterized by a series of harmonic peaks, has been presented, confirming the existence of this unique signature of acoustic oscillations in the early universe. This is an important confirmation of standard adiabatic models of structure formation, and thus of the process of constraining cosmological parameters based on increasingly precise measurements of the position and amplitude of these peaks by current and future CMB experiments.

The precision and extent of the angular power spectrum that is reported here already allow an accurate determination of several cosmological parameters with the assumption of only weak astrophysical priors. Assuming $0.45 < h < 0.90$, the CMB data tightly constrain the values of Ω_{tot} and n_s to lie close to unity and tightly constrain Ω_b to a value consistent with BBN.

Adding constraints from observations of Large Scale Structure and of type 1a supernovae, yields a value for the Hubble constant of $h = 0.67 \pm 0.09$, that is in good agreement with the HST key project final value of 0.72 ± 0.08 (Freedman et al 2000). These data also provide compelling evidence for the existence of both dark matter and dark energy. Including LSS, SN1a or a prior on the Hubble constant of $h = 0.71 \pm 0.08$ each yields $\Omega_\Lambda \approx 2/3$ and $\Omega_m \approx 1/3$.

REFERENCES

Preliminary analysis of Acbar data, J. Ruhl, 2001, private communication.

Bond, J. R. and Efstathiou, G., MNRAS, 226, 655(1987).

Bennett, C.L. et al. 1996, ApJ, 464, 1

J.R. Bond, A.H. Jaffe & L. Knox, ApJ, 533, 19-37, 2000. astro-ph/9808264

J.R. Bond, A.H. Jaffe & L. Knox, Phys. Rev. D, 57, 2117, 1998. astro-ph/9708203

J.R. Bond and A.H. Jaffe, Phil. Trans. R. Soc. London, 357, 57(1999), astro-ph/9809043.

Bond, J.R. et al., 2001, in preparation.

Borrill J. 1999, Proc. of the 3K Cosmology EC-TMR conference, eds. L. Maiani, F. Melchiorri, N. Vittorio, AIP CP 476, 277

Church, S.E., Ganga, K.M., Ade, P.A.R., Holzapfel, W.L., Mauskopf, P.D., Wilbanks, T.M. and Lange, A.E. 1997, ApJ, 484, 523

Contaldi, C.R., Hindmarsh, M.B. and Magueijo, J., 1999, Phys. Rev. Lett. 82 679-682

Crill, B. et al., 2001, in preparation

de Bernardis, P., et al. 2000, Nature, 404, 955-959

de Bernardis, P., et al, 2002, ApJ, 564.

Efstathiou G., and Bond, J. R., MNRAS, 304, 75(1999).

Finkbeiner D.P. et al. 1999, ApJ, 524, 867.

Freedman W. L. et al, 2000, ApJ in press, preprint astro-ph/0012376.

Górski, K.M., Hivon, E. and Wandelt, B.D., in "Analysis Issues for Large CMB Data Sets", 1998, eds. A.J. Banday, R.K. Sheth and L. Da Costa, ESO(astro-ph /9812350), see also http://www.tac.dk/ healpix/

Jaffe, A., et al., 2001, Phys. Rev. Lett., 86, 3475-3479

Hanany, S. et al., 2000, ApJ, 545, L5-L9

Hivon, E., Gorski, K.M., Netterfield, C.B., Crill, B.P., Prunet, S. & Hansen F., 2001, astro-ph/0105302, accepted in ApJ

Hu W., Sugiyama N. & Silk J., 1997, Nature, 386, 37

James,G.L."Analysis and design of TE11 to HE11 corrugated cylindrical waveguide mode converters", *IEEE Trans. Microwave Theory and Techniques*, Vol. MTT-29, pp 1059-1066, 1981.

Lange, A.E., et al, 2001, Phys. Rev. D, 63, 042001

Lineweaver, C.H., et al. 1996, ApJ, 470:38-42.

Masi S., et al. 2001, ApJin press, astro-ph/0101539

Mauskopf, P. et al. 2000, ApJ, 536, L59

Miller, A. et al. 1999, ApJ, 524, L1

Murphy, J.A., Ruth Colgan, Creidhe O'Sullivan, Bruno Maffei, and Peter Ade. "Radiation Patterns of Multi-Moded Corrugated Horns for Far-IR space Applications". Preprint, TeraHz Technology Conference, 2001.

Netterfield, C. B., et. al. 1997, ApJ, 474, 47

Padin, S., et al., 2001, ApJ, 549, L1-L5

Peebles, P.J.E, and Yu J.T., 1970, ApJ162, 815

Piacentini, F. et al., 2002, accepted by ApJS

Prunet, S. et al., 2000, in "Energy densities in the Universe", Bartlett J., Dumarchez J. eds., Editions Frontieres, Paris - astro-ph/0006052

S. Perlmutter et al., ApJ, 517, 565(1999)

Riess et al., 1998, AJ, 116, 1009

Rao, S.M., D. R. Wilton, and A. W. Glisson,"Electromagnetic scattering by surfaces of arbitrary shape", *IEEE Trans. Antennas and Propagation*, Vol. AP-30, no. 3, pp 409-418, May 1982.

Schlegel D.J. et al. 1999, ApJ500, 525.

Stumpff, 1980, A&A Suppl, 41, 1.

Sunyaev, R.A. & Zeldovich , Ya.B., 1970, Astrophysics and Space Science 7, 3-19

Tegmark M. et al., 2000, ApJ530, 133.

Turok, N., Pen, U-L. and Seljak, U. 1998, Phys. Rev. D58 023506

Tytler, D. et al. 2000, Phys. Scr, submitted, astro-ph/0001318.

Wright, E.L., 1998, ApJ496, 1.

WOMBAT collaboration, 1998, see http://astron.berkeley.edu/wombat/foregrounds/radio.html.